Acta Biomaterialia 163 (2023) 78–90

Contents lists available at ScienceDirect

Acta Biomaterialia

journal homepage: www.elsevier.com/locate/actbio

Full length article

Understanding the inelastic response of collagen H fibrils: A viscoelastic-plastic constitutive model ☆

Fernanda F. Fontenele, Nikolaos Bouklas *

Sibley School of Mechanical and Aerospace Engineering, Cornell University, NY 14853, USA

a r t i c l e i n f o

Article history:
Received 30 March 2022
Revised 1 July 2022
Accepted 5 July 2022
Available online 12 July 2022

Keywords:
Collagen H fibrils
Fatigue loading
Plasticity
Viscoelasticity
Soft tissues

a b s t r a c t

Collagen H fibrils, which are the lowest level H fibrillar unit of organization of collagen, are thus of primary interest towards understanding the mechanical behavior of load-bearing soft tissues. The deformation of collagen H fibrils shows unique mechanical features; namely, their high energy dissipation is even superior compared to most engineering materials. Additionally, there are indications that cyclic loading can further improve the toughness of collagen H fibrils. Recent experiments from Liu at al. (2018) focused on the response of type I collagen H fibrils to uniaxial cyclic loading, revealing some interesting results regarding their rate-dependent and inelastic response. In this work, we aim to develop a model that allows interpreting the complex nonlinear and inelastic response of collagen H fibrils under cyclic loading. We propose a constitutive model that accounts for viscoelastic deformations through a decoupled strain-energy density function (into an elastic and a viscous parts), and for plastic deformations through plastic evolution laws. The stress-stretch response results obtained using this constitutive law showed good agreement with experimental data over complex loading paths. Ultimately we use the model to gain more insights on how cyclic loading and rate effects control the interplay between viscoelastic and plastic deformation in collagen H fibrils, and to extrapolate the results from experimental data, analyzing how complex cyclic load influences energy dissipation and deformation mechanisms.

Statement of significance

In this work, we develop a viscoelastic-plastic constitutive model for collagen H fibrils with the aim of analyzing the effects of inelasticity and energy dissipation in this material, and more specifically the competition between viscoelasticity and plasticity in the context of cyclic loading and overload. Experimental and theoretical approaches so far have not fully clarified the interplay between viscous and plastic deformations during cyclic loading of collagen H fibrils. Here, we aim to interpret the complex nonlinear response of collagen H fibrils and, ultimately, suggest predictive capabilities that can inform tissue-level response and injury. To validate our model, we compare our results against the stress-stretch data obtained from experiments of cyclic loaded single H fibrils performed by Liu et al. (2018).

1. Introduction

Many soft biological tissues that serve a load-bearing function, such as tendon, ligament and cartilage, are composed of hierarchically assembled collagen proteins. Fibrillar collagen is usually the main load-carrying component of these tissues and the way that it is connected, distributed and aligned determines the mechanical properties of the tissues throughout length scales [1–4]. Collagen H fibrils (up to 1cm in length, and 500μm in diameter [5]) are the lowest level of H fibrillar organization of collagen above the molecular level. They are composed by the ordered assembly of tropocollagen (TC) molecules (approx. 300nm in length, and 2nm in diameter) and are D-periodic with D = 67nm, as the length of a TC monomer is not an exact multiple of D but L = 4.46D, creating gaps of 0.54D and overlaps of 0.46D [6,7].

The structure and the mechanics of collagen H fibrils, in the context of monotonic and quasistatic loading, have been extensively studied [8–10]. Yet, understanding the cyclic response of collageneous tissues throughout scales is also highly relevant for both

☆ Part of the Special Issue on the Mechanics of Cells and Fibers, guest-edited by Professors Amrinder S. Nain, Derrick Dean, and Guy M. Genin.

* Corresponding author.
E-mail address: nb589@cornell.edu (N. Bouklas) .

https://doi.org/10.1016/j.actbio.2022.07.011
1742-7061/

physiological loading and overload-induced injury. However, even though significant investigations have been performed at the tissue level [11–15], the cyclic response at the fibril level and below has not been explored as widely. In fact, it is known that some mechanical properties of collageneous tissues may vary substantially across length scales. Studies have reported that collagen fibrils have much smaller Young's modulus and much larger viscosity than collagen molecules [16], and that the fracture strain significantly decreases from collagen fibrils to the tissue level [17].

Studies at different levels of tissue hierarchy (molecule, fibril, fiber, fascicle and tissue) have shown that the level of applied deformation affects collagen degradation, which in turn, influences the mechanical properties of the tissue [18–20]. Additionally, the mechanisms underlying the rate-dependent deformation of collagen fibrils are not clearly understood and are bound to have a significant effect on their degradation. Regarding the deformation of a single collagen fibril, viscoelastic [21,22] and plastic deformations [23], as well as the presence of back stress [21] have been previously identified. The elastic deformation has been attributed to the stretching of the collagen molecules [24]. The viscous deformation, on the other hand, has been attributed to the rearrangement of collagen molecules and other mechanisms beyond the collagen molecule, such as the rearrangement of the water molecules inside the fibrils [21,22,25] and to the dynamics of hydrogen bonds between molecules [22]. As a mode of plastic deformation, discrete plasticity has been identified in fibrils in an experimental setting [23,26–29], pointing to the sliding of sub-fibril constituents as the cause to inelastic deformations and energy dissipation. Some studies suggest that the origin of plastic deformation in fibrils is due to the slip between two tropocollagen molecules with the rupture of covalent bonds [30,31]. The presence of hardening and back stress associated with plastic deformation has also been identified in some experimental studies [21,25].

Nevertheless, accurate modeling predictions of experimentally observed rate-dependent responses at the fibril level are still challenging. Coarse-grained simulations have been performed to analyze the mechanics of collagen fibrils at the nanoscale level allowing sub-fibril resolution [16,32]. These models were extended by Tang et al. [2] in a multiscale setting that employed continuum formulations in a rate-independent setting. There, a strain-energy density function was formulated to characterize the hyperelastic response of collagen fibrils, in addition to a plastic evolution law to characterize the permanent deformation of fibrils, as part of a multiscale informed model for collageneous tissue. They carefully connected the mechanisms of deformation observed at molecular level to the change in stiffness of fibrils, and selected functions for the model that could capture these features very well, however, the study was limited to monotonic loading without accounting for rate effects.

Rheological models have also been largely used as a way to create and interpret constitutive models for elastic, viscous and plastic nature of biological [33] and other soft materials [34–37]. Some models are not continuous and make use of Heaviside functions to describe the difference between loading and unloading curves [33]. As it is more challenging for models that employ discontinuous functions for loading and unloading to have a clear physical interpretation, Silberstein and Boyce [34] investigated the response of Nafion, and introduced continuous functions to represent the deformation of polymers in cyclic loading. Even though the material system is different than collagen fibrils, the phenomenology of the response is similar, involving elastic, viscous and plastic components along with the presence of back-stress.

To better understand how collagen fibrils respond to cyclic loading and at the same time be able to predict more complex loading paths, a constitutive model has to be formulated that can capture the complex interaction of viscoelastic and plastic deformation mechanisms present in this type of material. In this work we propose a constitutive formulation that aims to capture the rate-dependent response of collagen fibrils. More specifically, we intend to connect how cycling at different strain levels impacts the apparent stiffness, inelastic deformations and energy dissipation in collagen fibrils. To the best of our knowledge, no constitutive model has been developed that can capture both viscoelastic and elastoplastic effects in the response of collagen fibrils to non-monotonic loading. We use the experimental data provided in the work by Liu et al. [38] to validate our model.

This paper is divided as follows. In Section 2, we survey the mechanical response of type I collagen fibrils subjected to cyclic uniaxial tensile load as observed from experiments. We postulate that a viscoelastic-plastic model is sufficient to capture the observed responses. In Section 3, we specify the components of our constitutive model. We first review the kinematics of elastoplastic deformation, and outline the strain-energy density function which characterizes the viscoelastic behavior of the material. Next, we specify the elastic and the viscoelastic models. Finally, we specify the models for rate-independent plasticity, which include the plastic flow rule, yield criterion as well as isotropic and kinematic hardening. In Section 4, we first calibrate the constitutive model against the experimental data from the work by Liu et al. [38]. Then, we use the constitutive model to uncover the relationship between cyclic loading and so-called overload. In Appendix A, we outline the equations used to calculate the stress for the specific constitutive model in this work, and in Appendix B, we detail the numerical integration of the viscoelastic and plastic equations. In Appendix C we show results for an alternative set of parameters.

2. Collagen fibril response under cyclic load

The response of collagen fibrils to uniaxial tension is highly nonlinear. Undeformed collagen fibrils are usually found in a crimped (wavy) state, deviating from a perfectly straight configuration. Because of that, the fibrils carry little load in the initial bending-dominated regime of the deformation. As the crimped fibrils approach a straight configuration the deformation becomes stretching-dominated. Following the nomenclature from the work by Liu et al. [38], this initial stiffening process is denominated "regime I". The next stage, "regime II", is characterized by a softening in the material. Finally, the last stage, "post-regime II" defines the region in which the material has a secondary stiffening, preceding failure.

When the collagen fibril is subjected to cyclic loading, the stress-strain response becomes significantly more complex. The unloading of the material is nonlinear, as we can verify in Fig. 2 in Liu et al. [38]. In that work, Liu et al. investigate the response of reconstituted collagen fibrils to cyclic loading. The fibrils, composed of type-I collagen, are extracted from calf skin under partially hydrated conditions of 60% humidity. They subjected the fibrils individually to a first series of cyclic uniaxial tests within the limits of each regime – "regime I", "regime II", "post-regime II" – (termed series-1), let the material rest for 60 minutes and repeated the load for each regime after the recovery time (termed series-2). The reloading curves of the cycles evolve showing some possible ratcheting effect as the average strain increases with cycles until it reaches a stable value [39]. This equilibration is evident as curves that belong to the final cycles of the same series are overlapping. Additionally, we note that the inelastic strain is partially recovered as the fibrils are allowed to rest, showing evidence of viscoelastic deformation. However, part of the inelastic strain is not recovered which point to plastic deformation. We can observe that in Fig. 3 in Liu et al. [38], as the first cycle of series 1 does not overlap with the first cycle of series 2.

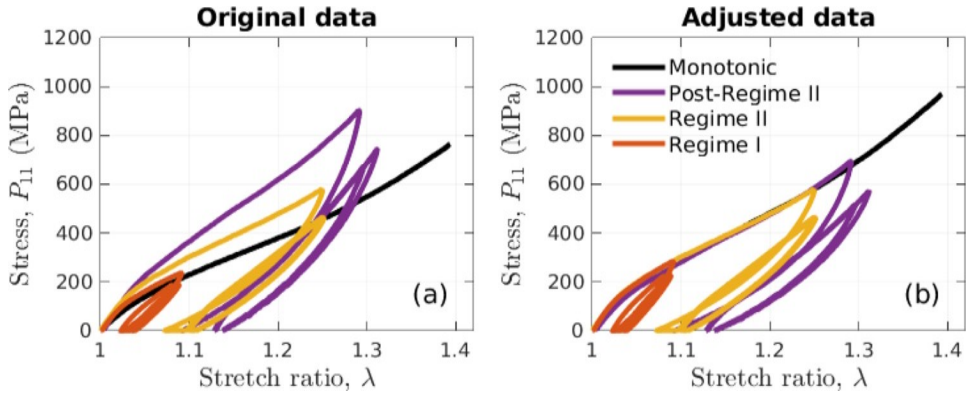

Fig. 1. Engineering stress-stretch curve obtained from experiments on four distinct collagen fibrils subjected to uniaxial stress load, for monotonic loading and for a number N_c of cycles of loading at different strain levels (regime I, II and post-regime II), where $N_c = 10$ for regime I and post-regime II, and $N_c = 20$ for regime II. For regimes with $N_c = 10$, only curves 1, 9 and 10 are shown, and for regimes with $N_c = 20$, only curves 1, 2, 8 and 10 are shown, reporting the available experimental data, which was provided by Liu et al. [38] . Each fibril is only subjected to one level of loading. (a) shows the original stress-stretch data found in [38] . (b) shows the stress-stretch curves from the data adjusted for the updated values of diameters of the fibrils. The curve for regime II is the reference curve and the diameters of the fibrils for the other curves were multiplied by the following factors: $\alpha = 0.89$ for the monotonic curve, $\alpha = 0.91$ for Regime I and $\alpha = 1.14$ for Post-Regime II.

In Fig. 1a, we show data from four separate experiments, each corresponding to a distinct collagen fibril specimen, as presented in the work by Liu et al. [38]. These data points correspond to series-1 cyclic loading from regime I, regime II, post-regime II, and a monotonic uniaxial tension experiments. In this order, each cyclic regime corresponds to an increasing value of maximum applied stretch in the loading direction. To clarify, each of the four fibrils was tested only on one regime. The fibril diameters are very small and each measurement of the diameter from imaging data comes with significant uncertainty. This uncertainty in the measurement of the diameter, when squared to calculate the stress values from the measured force, has a significant effect on the stress values, and, consequently, we hypothesize that it may have resulted in the lack of overlap between the curves in Fig. 1a. The authors of [38] provided us with measurements from imaging data that showed that there were uncertainties with the measurements from the collagen fibril diameters corresponding to the specimens used in the monotonic, regime I and post-regime II experiments. Adjusting in line with the updated imaging measurements and calculating from the raw data of the measured force that the authors of [38] provided (updating the fibril diameters), we obtain the stress-stretch response for these four separate tests that we compile in Fig. 1b. The curve for regime II is taken as the reference curve, since the specimen tested in this regime had the most accurately reported diameter. Indeed, this hypothesis is validated as, after adjusting the fibril diameters, we observe a significant overlap of the stress-stretch curves for the monotonic tensile loading portion of the four experiments. We note that the slight deviation of the initial portions of the four curves could be due to experimental setup leading to different initial curvatures of the fibrils.

With all these features in mind, we seek for a constitutive model that captures the stretch-stress response of type I collagen fibrils under uniaxial tensile load, for monotonic load as well as cyclic load within all three regimes of deformation. Thus, we formulate a phenomenological model which accounts for viscoelastic and elastoplastic response at finite deformations.

3. A viscoelastic-plastic constitutive model for collagen fibrils

In this section, we present a brief discussion on kinematics, followed by the description of our choices of models for the elastic, viscous and plastic response of collagen fibrils based on the observations from cyclic loading of collagen fibrils discussed in Section 2.

3.1. Kinematics

Consider a homogeneous body with reference configuration $\mathcal{B}_0$ at some fixed time t_0. Let X be the position vector of a material point in $\mathcal{B}_0$ and x be the position vector of a material point in the current configuration $\mathcal{B}$ at time t . The deformation of the material from $\mathcal{B}_0$ to $\mathcal{B}$ is defined by the motion

$$x = \chi(X, t) = X + u(X, t), \tag{1}$$

where u corresponds to the displacement of the material point. The deformation gradient in $\mathcal{B}_0$ is defined as

$$F = \nabla_X x = \frac{\partial\, \chi(X,t)}{\partial X}, \tag{2}$$

with components $F_{ij} = \partial \chi_i / \partial X_j$, where $\nabla_X(\bullet) = \partial(\bullet)/\partial X$ is the gradient operator in the reference configuration. In the context of elastoplasticity, we assume a standard multiplicative decomposition of the deformation gradient [40], i.e.

$$F = F^e F^p, \tag{3}$$

where F^e and F^p represent the elastic and plastic parts of the deformation gradient, respectively. Note that we make $J = J^e$, with $J \equiv \det F$ and $J^e \equiv \det F^e$, which follows from the assumption of plastic incompressibility of the material, i.e. $J^p \equiv \det(F^p) = 1$. The decomposition in (3) introduces an intermediate configuration, which we denote as $\mathcal{B}_i$. The plastic part of the deformation gradient maps the material point from $\mathcal{B}_0$ to the $\mathcal{B}_i$, and the elastic part maps the material point from $\mathcal{B}_i$ to $\mathcal{B}$. We take the intermediate configuration to be isoclinic [41], so as the symmetry axis of the material in $\mathcal{B}_i$ coincides at all times with the initial symmetry axis in $\mathcal{B}_0$. Because of the decomposition of F in (3), we can define elastic and plastic strain measures separately in terms of F^e and F^p, respectively. Here, we use the elastic Green strain tensor

$$E^e = \frac{1}{2}(C^e - I), \tag{4}$$

where $C^e = F^{eT} F^e$ is the elastic Cauchy-Green deformation tensor, and I is the second-order identity tensor.

Finally, we define the rates of deformation of the material. The velocity gradient tensor in $\mathcal{B}$ is defined as $L = \partial v / \partial x$, where $v = \dot{\chi}(X, t)$ is the velocity field. We note that hereon a dot over a tensor denotes the material time derivative of the tensor. In what

follows, the velocity gradient takes the form $L = \dot{F}F^{-1}$, and by employing the decomposition in (3), it is also expressed as

$$L = F^{e-1}\dot{F}^{e} + F^{e}L_{i}^{p}F^{e-1}, \quad L_{i}^{p} = \dot{F}^{p}F^{p-1}, \tag{5}$$

where L_{i}^{p} is the velocity gradient in the intermediate configuration.

3.2. Strain energy density considerations

Considering the nanostructure of collagen fibrils [7,8,10], known mechanisms for inelastic deformations [21,22,25,30], and features of the response of cyclically loaded collagen fibrils discussed in Section 2, we choose to model this material in the context of coupled viscoelasticity and elastoplasticity at finite deformations.

We consider that the viscoelastic constitutive behavior of the material can follow a specified strain energy density function ψ that accounts for the preferential direction of alignment of the microstructure of collagen fibrils, in the direction of the fibril itself [7,8,30,42] We assume that the energy-function ψ can be additively decomposed into an elastic part ψ^{e} that considers the equilibrium response and a viscoelastic part ψ^{v} that accounts for rate-dependence, as follows

$$\psi = \psi^{e} + \psi^{v}. \tag{6}$$

The elastoplastic response of the material is formulated assuming a rate-independent approach; we effectively assume that all rate effects are accounted for by viscoelasticity. The yield surface is defined from a yield function $\bar{\Phi}$ considering isotropic and kinematic hardening, and the direction of the plastic flow is defined based on an associative flow rule.

3.2.1. Elastic equilibrium response

The elastic equilibrium response of the material, defined with respect to the isoclinic intermediate configuration, is assumed to comply with a strain-energy density function $\psi^{e}(E^{e}) = \hat{\psi}^{e}(C^{e})$. It follows that the symmetric (second) Piola-Kirchoff stress is

$$S = \frac{\partial \psi^{e}}{\partial E^{e}}. \tag{7}$$

In this work, we assume that the strain-energy density function $\hat{\psi}^{e}$ characterizing the purely elastic deformation is a transversely isotropic invariant of C^{e}, with symmetry axis a_0, which is the unit vector in the reference configuration that represents the axial direction of the collagen fibrils. Thus, we can write the function $\hat{\psi}^{e}$ in the form Ericksen and Rivlin [43], Spencer [44]

$$\hat{\psi}^{e}(C^{e}) = \bar{\psi}^{e}(I_1, I_2, I_3, I_4, I_5), \tag{8}$$

where $I_1 = \mathrm{tr}C^{e}$, $I_2 = \frac{1}{2}[(\mathrm{tr}C^{e})^2 - \mathrm{tr}(C^{e})^2]$, $I_3 = \det C^{e}$, $I_4 = a_0 \cdot C^{e}a_0$, and $I_5 = a_0 \cdot (C^{e})^2 a_0$ are the set of principal scalar invariants of C^{e} and pseudo-invariants of C^{e} and $a_0 \otimes a_0$, where the symbol $\otimes$ represents the dyadic product between tensors of any order. Consequently, to find the elastic equilibrium part of stress in the fibrils, we use (7) and (8) and calculate $S^{e} = \partial\psi^{e}(E^{e})/\partial E^{e} \equiv 2\partial\hat{\psi}^{e}(C^{e})/\partial C^{e}$.

We choose a specific energy-function for (8) to characterize the purely elastic equilibrium deformation of the material, which we denote as ψ^{e}. We select a function that is able to capture the main aspects of the recoverable rate-independent deformation of the collagen fibrils, as described in Section 2. Following the work by Tang et al. [2], we use a Neo-Hookean model with the shear modulus depending on the axial direction of the fibrils a_0 through the fourth invariant I_4. Here we take the compressible form of the Neo-Hookean model as follows

$$\bar{\psi}^{e} = \frac{\mu(I_4)}{2}(I_1 - 3 - 2\ln J) + \frac{\beta}{2}(J-1)^2, \tag{9}$$

where $\mu = \mu_0 f(I_4)$ is the varying shear modulus, μ_0 is a constant and $J = \det F$. The parameter β represents the bulk modulus, which is assigned to a large value ($\beta >> \mu_0$) in this work, in order to approach incompressibility. The function $f(I_4)$ is defined as

$$f(I_4) = a_1 \tanh[a_2(I_4 - 1)] + a_3 \exp[a_4(I_4 - I_0)], \tag{10}$$

where a_1, a_2, a_3 and a_4 are material constants to be fitted, and I_0 is a material constant that represents the secondary stiffness of the fibril in the stage of deformation preceding failure. The hyperbolic function in f captures the evolution of the stiffness as the fibrils are stretched from the crimped state, characterizing the "toe" region [2].

We note that the formulation of the elastic equilibrium part of the stress S^{e}, calculated using the energy-function in (9) can be found in Appendix A.

3.2.2. Non-equilibrium response

The model for the viscoelastic response of the material, similar to the model for the elastic equilibrium response, is defined with respect to the isoclinic intermediate configuration through a strain-energy density function ψ^{v} based on the decomposition from (6). We follow the work by Linder et al. [45] and Wang et al. [46] and adopt a viscoelastic model first introduced for rubber-like materials. We take a strain-energy density function of the type $\hat{\psi}^{v}(C^{e}, A)$, where we include an internal variable A to account for the dissipative viscous overstress related to the viscoelastic deformations. The specific viscoelastic strain-energy density function is given by

$$\hat{\psi}^{v} = \frac{1}{2}\mu_{v}\,(A : \bar{C}^{e} - 3) - \ln(\det A), \tag{11}$$

where A is a symmetric tensorial quantity [45]. Here, the bar over the tensor C^{e} denotes that we are using the volume-preserving (distortional) part of the elastic right Cauchy-Green tensor, which is given by $\bar{C}^{e} = \bar{F}^{eT}\bar{F}^{e}$, where $\bar{F}^{e} = J^{e-1/3}F^{e}$.

The evolution of tensor A in (11) is given by

$$\dot{A} = \frac{1}{\tau}(\bar{C}^{e\,-1} - A), \quad A(X, t_0) = I, \tag{12}$$

with τ being a single relaxation timescale and I is the second-order identity tensor. When $C^{e\,-1} = A$, the system is expected to reach equilibrium and be fully relaxed. We note that the viscous overstress S^{v} can also be calculated using (7), along with (11), i.e. $S^{v} = \partial\psi^{v}(E^{e}, A)/\partial E^{e} \equiv 2\partial\hat{\psi}^{v}(C^{e}, A)/\partial C^{e}$. This calculation can be found in the Appendix A.

3.2.3. Plastic response

We choose a rate-independent plasticity model based on the idea that the slip systems in the collagen fibrils lie on the direction of the symmetry axis a_0 [47] of the nanostructure of the fibrils, following observations of discrete plasticity from experiments and coarse-grained simulations, as discussed in the introduction. Thus, the yield function is defined as the deviatoric part of the elastic Mandel stress ($\Sigma^{e} = C^{e}S^{e}$) projected onto the slip direction a_0

$$\bar{\Phi}(\Sigma^{e}, \beta^{p}) = \bar{\sigma}_{y}(\bar{\varepsilon}^{p}) = 0, \quad a = a_0 \cdot (\Sigma^{e} - \beta)^{d} a_0, \tag{13}$$

where the superscript d denotes the deviatoric part of the tensor to which it refers. The tensor β is the back-stress, which is included by means of a kinematic hardening law, and $\bar{\sigma}_{y}$ is the yield stress given as a function of the accumulated plastic strain $\bar{\varepsilon}^{p}$ (isotropic hardening). We assume that the material obeys the associative flow rule

$$L_{i}^{p} = \dot{L}_{t} M_{i}^{p}, \quad M_{i}^{p} = \frac{\partial \bar{\Phi}}{\partial \Sigma^{e}} = (a_0 \otimes a_0)^{d}, \tag{14}$$

where $\dot{L}_{t} \geq 0$ is the plastic multiplier.

We add isotropic and kinematic hardening models in order to account for a possible evolution of the yield surface. As discussed in Section 2, the unloading of the fibril becomes significantly nonlinear as it approaches a stress-free state. This can be caused by

a back-stress, which is accumulated by the pile-up of dislocations during plastic deformation [48], and which assists the deformation of the fibril in the reverse direction during unloading [34]. Consequently, the yield stress is reduced in the reverse deformation, what is known as the Bauschinger effect. In the context of collagen fibrils, dislocations can be interpreted as sliding defects between sub-fibril blocks [30,49].

To characterize the evolution of the back-stress, we use the kinematic hardening Armstrong-Frederick model [50]

$$\overset{\circ}{\beta} = \dot{L}_t \hat{\beta} = \overset{\nabla}{\beta}, \quad \overset{\nabla}{\beta} = \dot{H}(\bar{p}) M_i^p - b\beta, \tag{15}$$

where b is a material constant. We select this model because it is nonlinear, and nonlinear kinematic hardening laws can allow capturing ratcheting effects during cyclic loading. The term $b\beta$ in the above equation is there to account for the saturation of the back stress, and $(\overset{\circ}{\bullet})$ represents the Jaumann rate of a tensor, which is an objective rate defined as

$$\overset{\circ}{\beta} = \dot{\beta} - \dot{\Omega}^e\beta + \beta\dot{\Omega}^e, \tag{16}$$

for the back-stress, where $\Omega^e = \dot{R}^e R^{eT}$ and R^e is the rotation tensor resulting from the polar decomposition of the elastic deformation gradient, i.e. $F^e = R^e U^e$. We choose the following function for $H(\bar{p})$

$$H = H_0 + k_L \bar{p} + k_E \exp(k_P \bar{p}), \tag{17}$$

where H_0, k_L, k_E and k_P are parameters to be fitted.

In what follows, we choose to model the isotropic hardening with a linear-exponential function proposed by Gasser and Holzapfel [47]

$$y = \sigma_0 + h_E \bar{p} + h_E \exp\left(-\frac{\bar{p}}{\sigma_0}\right), \tag{18}$$

where σ_0 is the initial yielding stress, h_L, h_E and σ_0 are other material parameters. The addition of an isotropic hardening model, such as (18), to the plasticity model may be very important to the constitutive model as it helps balance the amount of ratcheting induced by the kinematic hardening throughout the cycles, until it possibly reaches a constant value.

We note that the evolution of the plastic strain $\bar{p}$ is given by $\dot{\bar{p}} = \dot{L}_t$ where the plastic multiplier $\dot{L}_t$ is assumed to follow the Karush-Kuhn-Tucker loading/unloading conditions and the consistency condition, given the irreversibility of the plastic flow [47]. For more details on the plasticity model, refer to [47].

4. Results and discussions

In this section, using the constitutive model developed in the previous section, we first fit the experimental data by Liu et al. [38] corresponding to cyclic loading at different loading regimes. Second, we use the constitutive model, with the calibrated material parameters, to investigate the response of collagen fibrils subject to more complex loading paths. This exercise is performed as a means to provide insights into the interplay between plastic and viscoelastic deformations as fibril loading transitions between physiological cyclic loading to overload.

4.1. Model calibration

To calibrate the proposed material model we utilized the data from Liu et al. [38] with the adjustments discussed in Section 2. The data that we used in the optimization consists of four distinct experiments - as we discuss in Section 2 -, namely

- monotonic loading,
- series 1 in regime I (20 cycles),
- series 1 in regime II (10 cycles),
- series 1 in post-regime II (10 cycles),

presented in Figs. 1a, 2b (or 3b), 4b and 5b, respectively in Liu et al. [38]. Note that not all cycles are shown in these plots; e.g. when there are 10 cycles only the first, ninth and tenth cycles are shown; this choice is to showcase the level of cyclic loading where the response has almost stabilized. Here we choose to work only with data from "series 1" (following the nomenclature from Liu et al. [38]), to avoid experimental errors of manually stopping and restarting the loading which was necessary for obtaining "series 2" cycles. We note that the fibrils are assumed to reach an equilibrated unloaded state after series 1 loading cycles, and prior to initializing loading cycles for series 2. This loading scenario is similar to what we will examine in the next section.

The details on the stress calculations for the proposed constitutive model, and necessary for the optimization procedure, are included in the Appendix A. The parameters of the model were optimized using the fminsearch function on Matlab. The fminsearch function is based on an algorithm that follows the Nelder-Mead method for function minimization [51]. This method calculates the values of a function of n variables at n + 1 edges of a simplex and replaces the highest value [52]. The inputs for fminsearch are the function to be optimized (fun) and the initial guess for the parameters (x_0). We define fun as a function of a vector containing the error between the values of the first Piola-Kirchhoff stress (P, as defined in Eq. (A.5)) obtained from the data points and the values of the first Piola-Kirchhoff stress calculated from the constitutive model. More specifically, we take fun to be a weighted sum of the Maximum Difference and Mean Square Error (MSE), i.e. the maximum value in the error vector and the square root of the average value of the squared entries of the error vector, respectively. The initial guess for the parameters is selected by following a multi-start procedure manually.

We first define ranges where we expect to find the most fundamental parameters being optimized. For instance, the shear moduli (μ_0 and μ_V, respectively) were expected to be inside an interval between zero and the initial Young's moduli (E_1) reported in [38], and the initial yielding stress (σ_0) was expected to be between zero and the maximum stress in the data in the direction defined in the yield criterion. Other additional parameters in the model, such as constants in the hardening laws, were defined in ranges near zero. We then select different sets of values of x_0 within the ranges defined and calculate the initial error that each of these sets yields. Next, we take the set that yields the smallest error to initialize the optimization procedure with fminsearch. We performed a sensitivity analysis on a subset of the parameters (H_0, k_L, k_E, k_P, h_L, h_E, σ_0) that allowed us to identify some parameters that could be removed from the model without significantly influencing the error. Finally, we run the optimization process again for this smaller set of parameters and determined the final values of the parameters.

First, we optimized the material parameters using all four experimental datasets (corresponding to series-1 cycles from the four experiments) simultaneously. The optimized parameters for this case are reported in Table 1. The strain rate is considered to be $4e-3s^{-1}$, following the experiments in [38], and the increment of the stretch imposed during loading is of $\dot{L}_t^{\text{load}}\Delta t = 1.5e-4$; consequently, $t_{\text{time}}^{\text{load}} = 0.375s$. The fit for the stress-stretch response of the collagen fibrils from our proposed model and the experimental data are presented in Fig. 2. The black dots represent the experimental data from Liu et al. [38] and the dashed orange lines represent the values calculated using the constitutive model formulated in this work for the optimized parameters summarized in Table 1. We observe from these plots that the optimized set of material parameters for the constitutive model leads to a satisfactory fit towards the experimental data for all four experiments (Fig. 2a–d) for the monotonic, regime I, regime II and post-regime II cases. Notably, not only the fit for the first cycle in each experiment is satis-

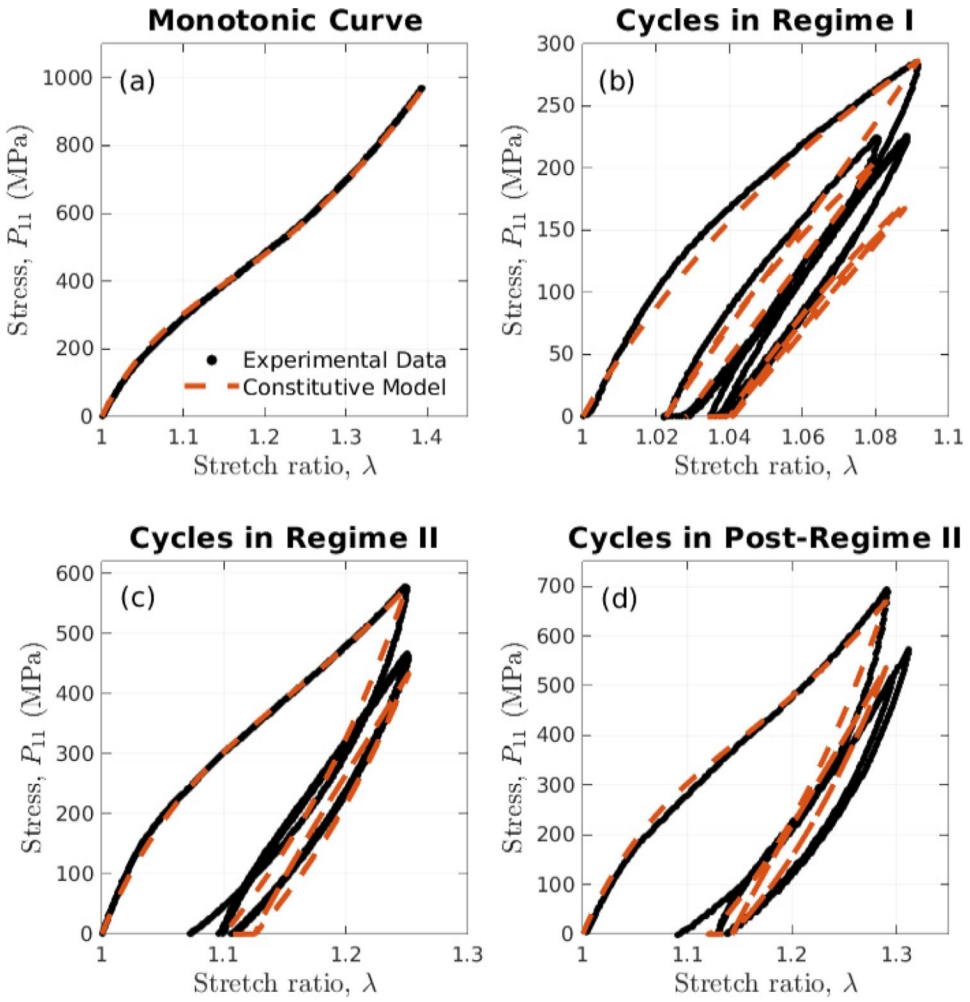

Fig. 2. Engineering stress-stretch curve of the hbrils subjected to uniaxial tensile load. The black circles represent the experimental data and the dashed orange line represents the results calculated from the constitutive model developed in this work. In this set of plots, the parameters are htted for all regimes simultaneously. a) shows the response of the hbril subjected to monotonic load with data provided in Fig. 1 in the work [38] . b) shows the response of the hbril subjected to 20 cycles of uniaxial load in series 1 (only cycles 1, 2, 8 and 20 are plotted) in regime I, following the data provided in Fig. 2 b in the work [38] . c) shows the response of the hbril subjected to 10 cycles of load in series 1 (only cycles 1, 9 and 10 are plotted) in regime II, following the data provided in Fig. 4 b in the work [38] . b) shows the response of the hbril subjected to 10 cycles of load in series 1 (only cycles 1, 9 and 10 are plotted) in post-regime II, following the data provided in Fig. 5 b in the work [38] . The parameters used to ht this curve are provided in Table C.1 .

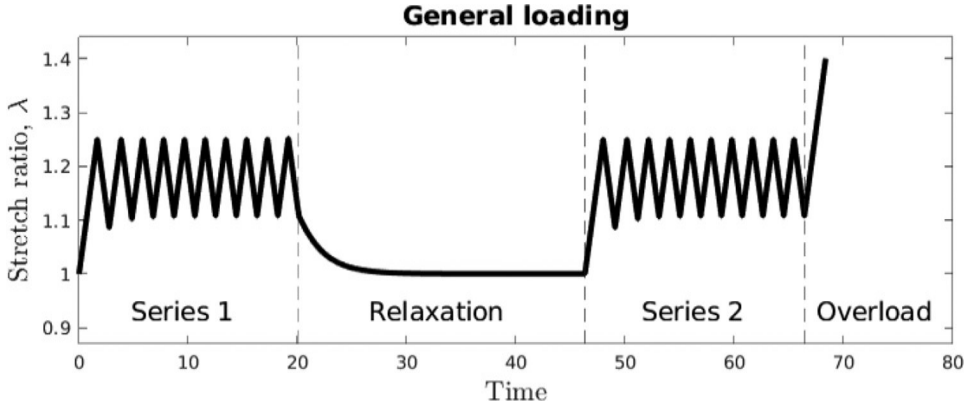

Fig. 3. Plot of stretch ratio λ vs time (non-dimensional, normalized by $10\frac{\Delta t}{\Delta t_{inc}}$) showing the general applied load in the results. The load is strain-controlled except during relaxation. This applied load sequence follows the applied load in the reference experiments by Liu et al. [38] . The load in this plot is shown for cycles in regime II ($\lambda^{max} = 1.25$).

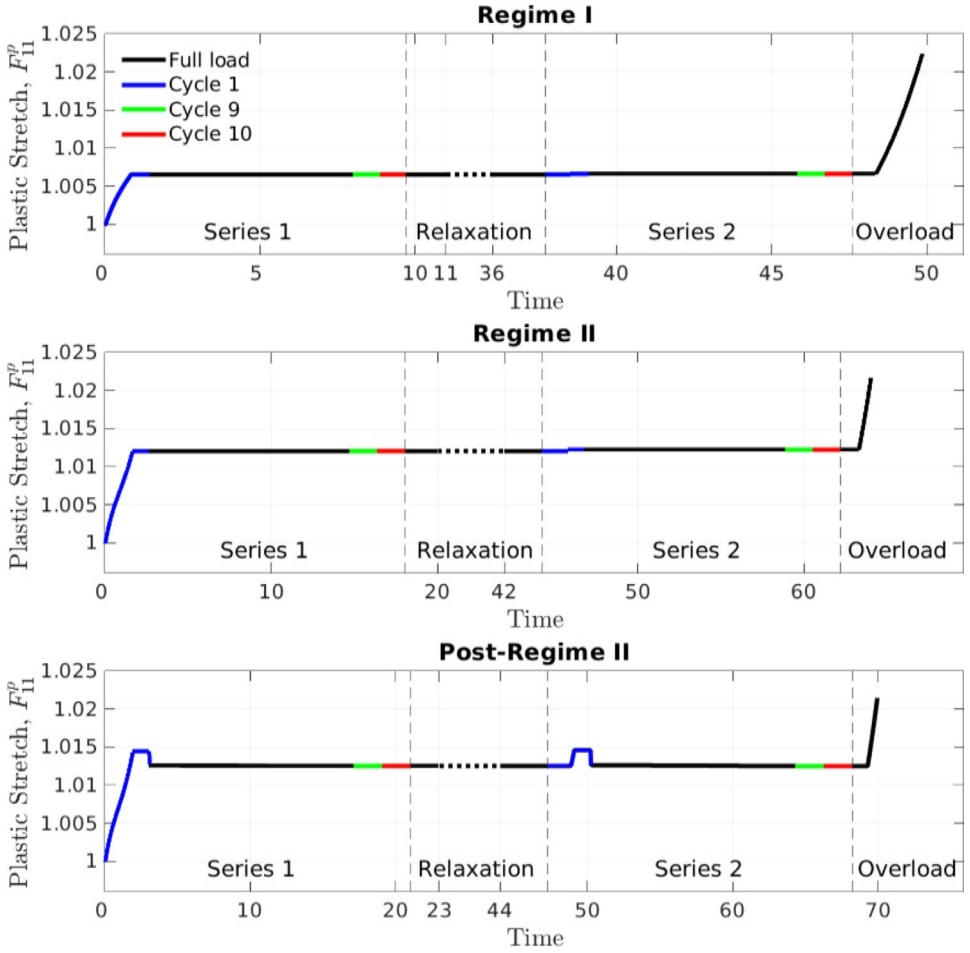

Fig. 4. Plots of plastic stretch (F_{11}^p) versus time (non-dimensional, normalized by 100 t_{time}^{ch}), which show the evolution of plastic deformation throughout loading. The applied load follows the general sequence of load: cycle series 1, relaxation, cycle series 2 and overload, as shown in Fig. 3 . The top plot shows the evolution of plastic stretch for cycles in regime I, the middle plot shows the evolution of plastic stretch for cycles in regime II and the bottom plot shows the evolution of plastic stretch for cycles in post-regime II.

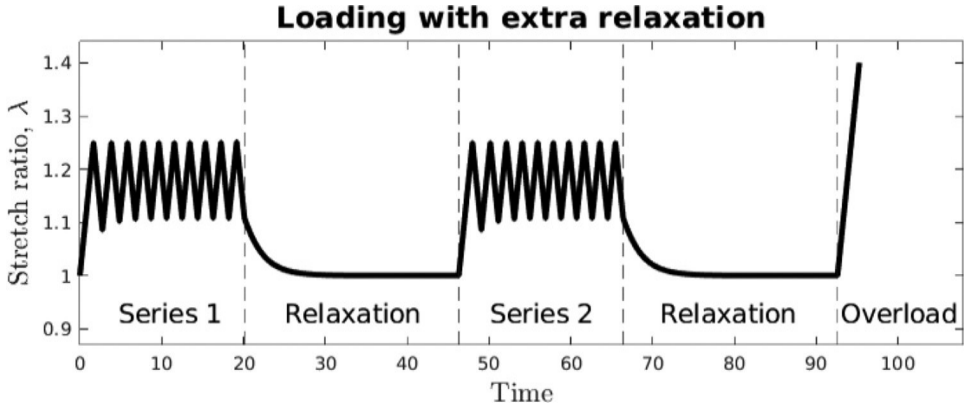

Fig. 5. Plot of stretch ratio λ vs time (non-dimensional, normalized by 100 t_{time}^{ch}) for an alternative load sequence, with an extra relaxation step compared to the general load in Fig. 3 . The load is strain-controlled except during relaxation. The load in this plot is shown for cycles in regime I ($\lambda_{max} = 1.25$).

Table 1
Parameters used to fit the experimental data of the uniaxial tension test provided in [38] to the constitutive model developed in this work. Here, we fit all tests (monotonic, and cycles in series 1 in regime I, II and post-regime II) simultaneously. The bulk modulus is kept at $\beta = 1e8$ MPa. The parameters not specified in this table were assigned to a value of zero.

Parameters optimized for all experiments												
H_0	b	t_{time}^{ch}/τ	μ_v(MPa)	μ_0(MPa)	σ_0(MPa)	h_E(MPa)	η_0	a_1	a_2	a_3	a_4	l_0
1.96e4	8160.0	0.0009	980.0	1740.0	10.0	0	0.0004	1.7344	0.2106	0.4408	-3.3313	0.9993

factory, but also the final cycles in Fig. 2b–d are also approximated well, especially considering the character of the response at that state, given that viscoelasticity dominates and leads to the hysteresis loop. On the other hand, yielding is not observed during the final cycles. We note that the value of the Young's modulus of the fibrils calculated from the shear moduli in the constitutive model (assuming incompressibility, $E \approx 2*(\mu_V + \mu_0)(1+0.5) \approx 8$GPa) is consistent with the data [38] and ranges reported in the literature [9]. However, we observe that, at the same time, the yielding stress parameter τ_0 is low relative to the maximum stress in all the regimes, indicating that yielding starts early on and the elastic deformation happens for only a small range of stretch values during loading in the first cycle. This observation does not apply for later cycles because as the yield surface evolves, following the hardening laws.

Nevertheless, the data of each experiment is collected from different fibril specimens, and we expect to encounter variability in some properties between fibrils such as the cross-link density and defect distribution [25,53], that can influence the deformation mechanisms described and eventually the optimized model parameters. For this reason, we also fitted each of the experiments individually and report the results in Appendix C. The optimized parameters in this case are outlined in Table C.1 and the stress-stretch plots are shown in Fig. C.1. The fit is slightly improved for this case, but considering that we have four distinct sets of parameters, this approach is not useful for predictive calculations. Thus, we will proceed with the former option of calibrating all available data concurrently, leading to one set of parameters, which as discussed previously yielded acceptable results. We note that as we optimize the model parameters and calibrate on the adjusted data of all experiments, it is straightforward to obtain the set of parameters that correspond to the original experimental curves simply by normalizing the stress-valued parameters of the model according to the adjusted fiber cross-sectional areas (as reported in Fig. 1).

4.2. Physiological loading and overload response

Overload of load-bearing orthopedic soft tissues such as tendon and ligament, commonly results from athletic activity [54,55], but the load sharing, dissipation and deformation, at different levels of hierarchy below the tissue level is not as transparent. Probing the tissue to cyclic loading does not directly provide information about deformation mechanisms and damage at lower scales. In this section we probe the effect of overload on the deformation mechanisms of collagen fibrils. Here, we define overload as an increased applied stretch following physiological activity (cyclic loading at a significantly lower maximum applied stretch). The constitutive model formulated in Section 3 allows us to assess results on the inelastic deformation for the overload response of collagen fibrils subjected to cyclic load in the three different regimes of deformation (regime I, II and post-regime II as described in Section 2). We discuss the contribution of plasticity and viscoelasticity to the inelastic deformation of fibrils, how plastic deformation evolves throughout the load cycles and how this evolution changes in different regimes. Additionally, we discuss the general aspects of overload of the fibrils, and how the overload response is influenced by the prior sequence of load applied.

Following the experiment in Liu et al. [38], we apply uniaxial tension in the axial direction of the fibrils. In these results, we take the direction e_1 to coincide with the axial direction of the fibrils ($e_1 \equiv a_0$). We impose the load by controlling the component of the deformation gradient in the direction $e_1 \otimes e_1$, i.e. $F_{11} := \lambda$. The general form of the sequence of load cycles applied, as investigated in this section, is shown in Fig. 3, following the nomenclature introduced by Liu et al. [38]. The first sequence of loading cycles is denoted here as series 1. For the first cycle in series 1, we start from the undeformed configuration $F = I$, and incrementally increase λ to a maximum λ^{max}, then we decrease λ until we reach a stress-free configuration ($S_{11} = 0$). We repeat this procedure until we complete 10 cycles. After 10 cycles in series 1, we start the relaxation process, in which we switch to a load-controlled setup. We keep the material at a stress-free state and calculate the corresponding stretch. As we impose a stress-free state, the stretch λ starts decreasing due to viscoelastic recovery, until we eventually no longer observe a significant change in the stretch value. Following, we impose the next sequence of loading cycles, referred to as series 2, which consists of 10 strain-controlled loading cycles applied similar to those in series 1. After the 10 cycles in series 2, we apply the so-called overload by incrementally increasing the stretch until we reach $\lambda = 1.4$. The maximum stretch in series 1 and 2 is $\lambda^{max} = 1.10$ for cycles in regime I, $\lambda^{max} = 1.25$ in regime II and $\lambda^{max} = 1.30$ in post-regime II. This choice of the overload stretch value $\lambda = 1.4$ is just taken to recapitulate an acute loading that follows cyclic loading activity that the tissue would experience (e.g. tendon or ligament).

We impose the general loading sequence showcased in Fig. 3 for all the three regimes by controlling the maximum stretch in the cycles (λ^{max}), and use the optimized model parameters (outlined in Table 1). We note that the relaxation time (or time to equilibration) following the series 1 cycles is different depending on the regime of loading that we are probing (for regime I, II and post-regime II). In Fig. 4, we plot the F^p_{11} component of the plastic stretch throughout the loading. The model predicts that the plastic stretch initially increases during the first loading cycle of series 1, and does not evolve significantly up until the overload. Similar observations hold for regime II and post-regime II, but for these regimes, slightly larger values of plastic stretch are reached prior to the overload. We note that for post-regime II, there is a step-type response for the plastic stretch in the first cycle of series 1 and 2. This happens because kinematic hardening (controlled by parameters b, H_0, k_L, k_E and k_P) shifts the yield surface of the material significantly and, during reverse loading, the material starts yielding while it is still being unloaded.

During cycles in series 1 and 2, the amount of plastic deformation during loading is higher if we cycle in higher regimes, as one would expect. For instance, $F^p_{11} \approx 1.006$ after loading the first cycle for regime I, $F^p_{11} \approx 1.012$ after loading the first cycle for regime II, and $F^p_{11} \approx 1.015$ for post-regime II, as can be seen in Fig. 4. As series 1 loading is identical to the loading from Fig. 2 for all regimes equivalently, we observe that the apparent inelastic stretch (viscoelastic and plastic) observed at the end of those experiments is significantly larger compared to just the plastic stretch F^p_{11}, highlighting the significance of the viscoelastic response. Notably, in Fig. 2 we observe an inelastic stretch, after the first cycle, of approximately 1.02 for regime I, 1.08 for regime II and 1.1 in post-regime II. This higher inelastic strain at higher levels of deformation is consistent with observations that molecular sliding occurs more significantly in regime II and post-regime II, and mostly in the first cycle of loading [38,56]. In contrast, in regime I, most of the deformation in the initial cycle of loading is due to the uncoiling of tropocollagen molecules [16], showing low levels of molecular sliding.

It is interesting that, overload leads to lower levels of plastic deformation as the fibrils were exposed to a higher stretch level during cyclic loading in series 1 and 2. For instance, after overload up to λ=1.4, the plastic stretch is $F^p_{11} \approx 1.0225$ for regime I, $F^p_{11} \approx 1.0217$ for regime II and $F^p_{11} \approx 1.0214$ in post-regime II. We postulate that this is the effect of the inelastic strains due to viscoelasticity, which we have already shown are not negligible and are increasing as higher stretch levels are obtained during cyclic loading in series 1 and 2. To verify this, we modify our cyclic load profile and introduce a relaxation step after series 2 (the load pro-

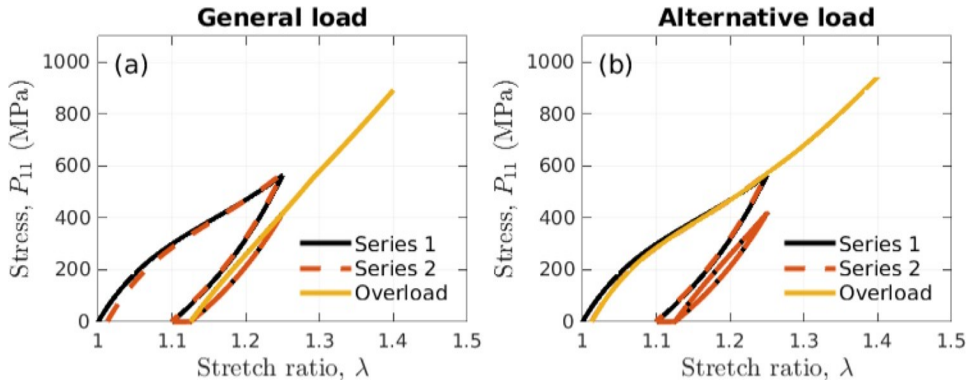

Fig. 6. Stress-stretch curve for a fibril subjected to cycles in regime II following a) the general sequence of load (described in Fig. 3) and b) an alternative sequence of load with an extra relaxation step which follows series 2 (described in Fig. 5).

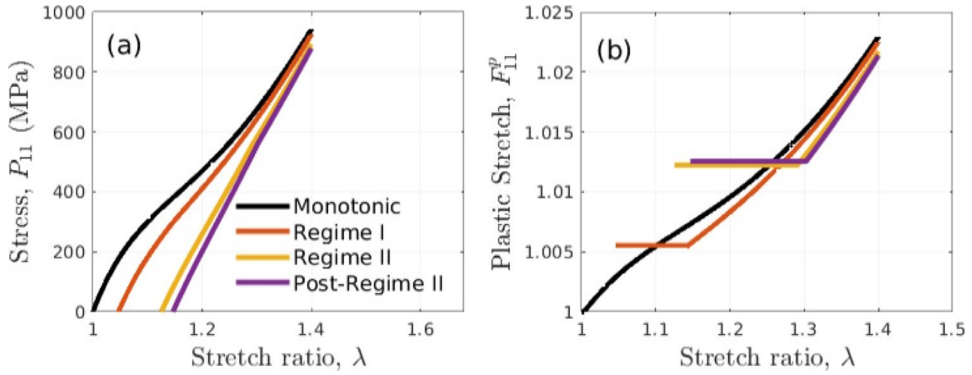

Fig. 7. Overload response to the general loading (Fig. 3) for stretch up to $\lambda = 1.4$. a) Shows a stress-stretch plot of the overload curves for fibrils cycled at different regimes and for monotonic load. The stress at $\lambda = 1.4$ for each curve is: monotonic, regime I (925.3MPa), regime II, and post-regime II. b) Shows the evolution of the plastic stretch in the fibrils direction for each curve in (a). The plastic stretch at $\lambda = 1.4$ for each curve is: monotonic, regime I, regime II, and post-regime II.

fibrille is described in Fig. 5). From that, we can anticipate that relaxation will influence the overload response by diminishing the viscoelastic contributions to the inelastic stretch. To observe this influence more clearly, we plot in Fig. 6a the stress-stretch response including the overload curve for a fibril subjected to the general loading (described in Fig. 3), and in Fig. 6b, the stress-stretch response including the overload curve for a fibril subjected to the alternative loading with an extra relaxation step (described in Fig. 5). Both series 1 and 2 load cycles are in regime II for the general loading and the alternative loading profile. We note that the overload response following immediately series 2 cycles is different than the overload response after relaxation, not only in the tangent modulus, here defined as the slope of the stress-stretch ratio curve, but also in the final stress at $\lambda = 1.4$ ($P_{11} \approx 900$MPa in Fig. 6a and $P_{11} \approx 950$MPa in Fig. 6b). This verifies that the viscoelastic contribution of the inelastic stretch has a significant effect on various aspects of the material response, which are eventually eliminated through additional relaxation. When the value of plastic deformation after the cyclic loading is low, the overload curve for the material after relaxation is very close to the initial monotonic response in Fig. 2a.

In Fig. 7a we plot only the stress-stretch curve for the overload part of the loading, for monotonic loading and the overload curves for the general loading (see Fig. 3) for cycles in each regime (consistent with the loading in Fig. 6a). In Fig. 7b, we plot the plastic stretch versus the applied stretch for just the overload portion of the loading in Fig. 7a.

We can observe that series 1 and 2 cycling in different stretch regimes influence substantially the overload response and the accumulation of plastic deformations. From Fig. 7a, we note that if we cycle the material in regimes of higher deformations, such as in post-regime II, the final stress values in the material will be lower for the maximum overload stretch of $\lambda = 1.4$. And, equivalently, from Fig. 7b, that the final values of plastic stretch in the material will be lower for the maximum overload stretch of $\lambda = 1.4$.

In what follows, we analyze the overload response for the alternative applied loading (see Fig. 5). In Fig. 8a we plot only the stress-stretch curve for the overload part of the loading, for monotonic loading and the overload curves for the alternative loading (consistent with the loading in Fig. 6b). In Fig. 7b, we plot the plastic stretch-applied stretch curve for the overload curves in Fig. 7a. By comparing the plots in Fig. 7 to the plots in Fig. 8, we note that the trend in the overload response in the material changes as we add an additional relaxation step before overload. In Fig. 8a, we observe that the final values of stress are very close for all curves, with cycles in higher regimes yielding slightly higher stress values at $\lambda = 1.4$. And, in Fig. 8b, we observe that the final values of plastic stretch are very close for all curves, with cycles in higher regimes also yielding slightly higher plastic stretch values at $\lambda = 1.4$.

In the work by Liu et al. [38], they pointed out that, because significant molecular sliding causes inelastic deformation in the fibrils, cycling in higher strains improves some mechanical properties in the fibrils such as the tensile strength and toughness, as it increases the stiffness of the stress-stretch curve in regime II, ie. E_2. Given that, some questions that arise from the analysis of the experimental data on the cyclic response of collagen fibrils reported in their work are: Is all the inelastic strain observed in the fibrils coming only from viscoelastic deformations? If mechanisms

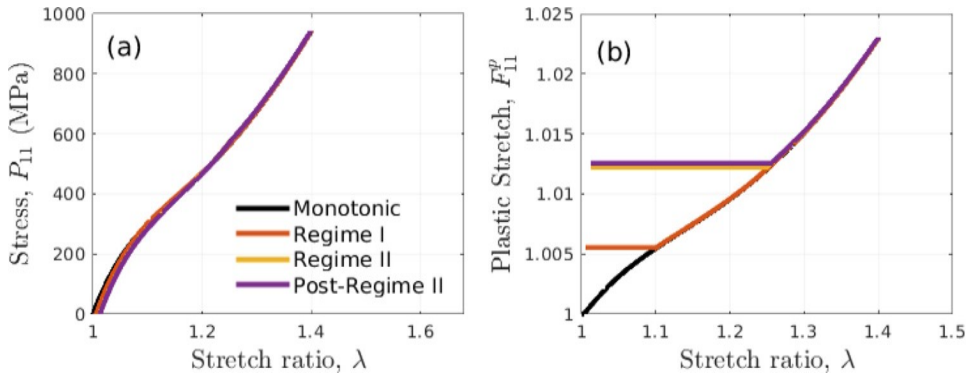

Fig. 8. Overload response to the alternative loading (Fig. 3) for stretch up to $\lambda = 1.4$. a)Shows a stress-stretch plot of the overload curves for fibrils cycled at different regimes and for monotonic load. The stress at $\lambda = 1.4$ for each curve is: monotonic, regime I, regime II, and post-regime II. b) Shows the evolution of the plastic stretch in the fibrils direction for each curve in (a). The plastic stretch at $\lambda = 1.4$ for each curve is: monotonic, regime I, regime II, and post-regime II.

of plastic deformation are also present, are they influenced by the amount of viscoelastic recoverable deformation?

As they suggest, after relaxation, the majority of the inelastic deformation is recovered. They imply that the hydrogen bonds broken during the initial stage of the deformation of the fibrils (uncoiling) are partly recovered. It has to be noted that their experiment does not focus on the extent of that recovery, as the plastic strains at the equilibrated response are not clearly reported. However, it is evident from the experimental data that not all of the inelastic strain is recovered after some relaxation time. That suggests that plastic deformation is present. In fact, from the results presented in our work, and more specifically in Fig. 4, we observe that not only the total inelastic deformation of the fibrils is more pronounced in the first cycle of loading and in regime II and post-regime II, but the plastic deformation has also higher values in the first loading cycle of series 1 and for cycles at higher strain levels. In addition to these remarks, the results we present in this paper show that the amount of viscoelastic deformation controls the amount of plasticity in the material. If the material undergoes significant viscoelastic deformation, the plastic deformation is expected to be smaller when the material is not allowed to relax. In this case, the stress values are also expected to be lower. We note that the calibration of the model parameters resulting from the optimization procedure suggested here might not be unique, which we further discuss.

These observations indicate that cycling at higher stretch levels immediately before overload can reduce the amount of plastic deformation as well as the stress levels by the end of the overload step. This interplay of repeated loading, relaxation, viscoelasticity and plasticity, can have a significant effect on suggesting loading profiles for exercise-based treatments for tendinitis, as one might wish to maximize loading while minimizing permanent deformation mechanisms.

In what concerns the total amount of plastic deformation induced in the material after the cyclic load, we observed that for regime I the plastic stretch calculated from the constitutive model is in line with the plastic stretch in [38]. For regime II and post-regime II, the amount of plastic deformation from the constitutive model is underestimated compared to the data in [38]. We have to note, that the referenced experimental work focused on the inelastic strains at the end of each cycle, and did not provide clear data on the plastic strain upon viscoelastic equilibration upon unloading as that was not the focus of the study. Some data was provided upon the end of cycling, as stretch decreased while fibrils were stress–free, but it was not clear whether those were equilibrated stretch values, that could confirm the plastic strains. Nonetheless, it was not possible to uniquely determine plastic parameters (yield stress, and constants in the kinematic and isotropic hardening models) for this constitutive model with great confidence given the experimental data provided. In fact, the data fits well when hardening is introduced to the plastic evolution law, however, we observed that the curve fits equally well for different ratios of kinematic and isotropic hardening variables. And even though these different sets of parameters yield similar stretch-stress curves, the final amount of plastic stretch varies significantly.

This challenge of determining the parameters in the plasticity model results from the fact that the experimental loading profiles are complex and involve many consecutive cycles of loading, which are very helpful in determining the viscoelastic part of the response. Additionally, it stems from the fact that the specific series of experiments were not designed to probe accurately the viscoelastic relaxation upon removal of the applied loads. Given the importance of further exploring the effects of plasticity and the dissipation of energy in collagen fibrils, we suggest experimental studies focusing on the determination of accumulation of plastic deformations without the consideration of complex cycling and resting loading profiles, such as plots of one individual cycle followed by relaxation and multiple experiments of the same category (cycles within the same regime) to quantify the uncertainty by means of parameter inference. We additionally suggest experiments be performed at different strain rates to investigate the rate dependence of the elastoplastic deformation.

5. Conclusion

In this work, we develop a constitutive model for collagen fibrils that can recapitulate the complex response to cyclic load, considering the combined effect of viscoelastic and plastic deformation mechanisms. The response of collagen fibrils to cyclic load has not been explored extensively, however, this type of loading is prominent in several biological tissues that provide a load-bearing function and are subject to damage accumulation and failure. The suggested viscoelastic-plastic model uses the additive decomposition of the equilibrium (elastic) and the non-equilibrium (viscoelastic) strain-energy density functions to dictate the elastic and the viscous deformation of the material. The plastic deformation is accounted through plastic evolution laws and includes the combination of isotropic and kinematic hardening models. The model allows the continuous observation of the parameters associated with the elastic, viscous and plastic deformation mechanisms that allow providing more insight towards understanding the response of collagen fibrils including their capacity to dissipate energy.

We optimize the parameters of our model to fit the data of four uniaxial tension tests provided by Liu et al. [38], which con-

sists of one stress-stretch plot for monotonic load, and three other stress-stretch plots for cyclic loading at different stretch levels. Even though we expect significant variability in the mechanical properties of different specimen of collagen fibrils, through an optimization procedure we were able to fit the the monotonic and cyclic experiments at all regimes simultaneously, and the results are reported in the results and discussion section. Utilizing the optimized constitutive model parameters, we studied the competition of viscoelastic and plastic deformation throughout cycling at different regimes, as well as following an overload. We note that the plastic deformation varies throughout cycles and that relaxation following cyclic loading affects how the material will respond to overload. We found that, when the material is allowed to relax prior to overload, it reaches higher values of stress and plastic stretch for the same maximum stretch imposed during the overload, implying that allowing for relaxation will likely lead to higher accumulated plastic deformations. On the other hand, when the material is subjected to cyclic load immediately before the overload, the amount of plastic deformation induced by overload is lower.

The proposed model allows us to interpret experimental results, and provides further insight on the rate dependent response of collagen fibrils. But additionally, forms the fundamental building block on which we plan to develop a truly multiscale constitutive model for tendon that will incorporate plasticity and viscoelasticity towards eventually studying the damage cascade that spans a hierarchy of features in tendon, and leads to macroscopic phenomena [57] such as kinking, collagen fiber rupture and ultimate failure.

Declaration of Competing Interest

The authors declare that they have no known competing financial interests or personal relationships that could have appeared to influence the work reported in this paper.

Acknowledgements

The authors gratefully acknowledge the discussions with Professor Ioannis Chasiotis and the data provided by him and his research team. The authors furthermore acknowledge the fruitful discussions with Professor Meredith Silberstein. The authors acknowledge the support by the National Science Foundation under grant no. CMMI-2038057.

Appendix A. Stress calculations

In this Appendix, we detail the stress formulations following the strain-energy density functions specified in Section 3. We use these expressions in the optimization algorithm to find the model parameters.

First, we calculate the symmetric Piola-Kirchhoff stress for the elastic deformations using (9) in (7), which yields

$$S^e = \mu_0 f'(I_4)(I_1 - 3 - 2\ln J)a_0 \otimes a_0 + \mu_0 f(I_4)\left(\bar{I} - \bar{C}^{e\,-1}\right) + \beta J(J-1)C^{e\,-1}, \tag{A.1}$$

where

$$f'(I_4) = a_1 a_2 \operatorname{sech}^2[a_2(I_4 - 1)] + a_3 a_4 \exp[a_4(I_4 - b)]. \tag{A.2}$$

Next, we calculate the second Piola-Kirchhoff stress for the viscoelastic deformations, i.e. the overstress from (11) in (7)

$$S^v = J^{-2/3}\mu_v \left(A - \frac{1}{3}\left(A : \bar{C}^e\right)\bar{C}^{e\,-1}\right). \tag{A.3}$$

Note that we also make use of the definition of the elastic Green strain tensor in (4).

Now, making use of the assumption of the additive decomposition of the strain-energy density function in (6), we can find that the total stress in the fibrils can be denoted as

$$S = S^e + S^v. \tag{A.4}$$

Nevertheless, the stress data provided by Liu et al. [38] is given in terms of the Engineering stress (applied force divided by the initial area of the specimen), which we denote as P. For this reason, we calculate the first Piola-Kirchoff stress in the reference configuration Ω_0. In the intermediate configuration Ω_i and in the reference configuration Ω_0, the first Piola-Kirchoff stress is calculated from

$$P_i = F^e S, \qquad P = P_i F_p^{-T}, \tag{A.5}$$

respectively.

Appendix B. Numerical integration

In this section we describe the numerical integration of the evolution of the internal variables representing the plastic and viscoelastic deformations of the material. We use an unconditionally stable implicit backward-Euler integration scheme.

First, following [50], we denote the numerical integration of the back-stress as

$$\beta_{n+1} = \bar{R}^{\text{fiber}}_{\text{time}}\beta_n \bar{R}^{\text{fiber}\,T}_{\text{time}} + \Delta t\, I_{t\,I^{\text{fiber}}_{\text{time}}}\hat{\beta}(\sigma_{n+1}, \beta_{n+1}, \alpha^p_{n+1}), \tag{B.1}$$

where $\bar{R}^{\text{fiber}}_{\text{time}}$ is the incremental elastic rotation defined as

$$\bar{R}^{\text{fiber}}_{\text{time}} = R^e_{n+1} R^{e\,T}_n, \tag{B.2}$$

and $I_{t\,I^{\text{fiber}}_{\text{time}}} = I_t \dot{I}^{\text{fiber}}_{\text{time}} t$ is the increment of the plastic parameter. The subscript $n+1$ indicates that the quantity is being calculated at the current time step while n refers to the previous time step.

Second, we find an update for the elastic deformation gradient at the current time step. We define an elastic deformation gradient trial as $F^{e\,tr}_{n+1} = F_{n+1}(F^p_n)^{-1}$. Then, we use the flow rule in (14) to find the update

$$F^e_{n+1} = F^{etr}_{n+1}\left(\bar{I} - I_{t\,I^{\text{fiber}}_{\text{time}}} M^p_i\right). \tag{B.3}$$

We finally get to solve a system of three equations using Newton-Raphson integration method. The three equations consist of the elastic deformation gradient update, yield criterion function and the back-stress update, as follows

$$\begin{cases} \text{Eq 1:} & F^e_{n+1} - F^{etr}_{n+1}\left(\bar{I} - I_{t\,I^{\text{fiber}}_{\text{time}}} M^p_i\right) = 0 \\ \text{Eq 2:} & \Phi(F^e_{n+1}, \alpha^p_{n+1}, \beta_{n+1}) = 0 \\ \text{Eq 3:} & \beta_{n+1} - \bar{R}^{\text{fiber}}_{\text{time}}\beta_n \bar{R}^{\text{fiber}\,T}_{\text{time}} - I_{t\,I^{\text{fiber}}_{\text{time}}} H_{n+1} M^p_i - b\beta_{n+1} = 0, \end{cases} \tag{B.4}$$

respectively. We note that the accumulated plastic strain at the current time step is calculated as $\alpha^p_{n+1} = \alpha^p_n + I_{t\,I^{\text{fiber}}_{\text{time}}}$ setting $\alpha^p_{t=0} = 0$.

Lastly, we outline the integration of the internal variable A representing the viscoelastic mechanism [45]

$$A_{n+1} = \frac{1}{1 + \Delta t^{\text{fiber}}_{\text{time}}/\tau}\left(A_n + \frac{\Delta t^{\text{fiber}}_{\text{time}}}{\tau}\bar{C}^{e\,-1}_{n+1}\right). \tag{B.5}$$

Appendix C. Alternate material parameter estimation procedure

Given the variability of the properties of specimen fibrils, in this section we present the results for the constitutive model with parameters optimized for each set of data individually. The optimized parameters are outlined in Table C.1.

In Fig. C.1, we show the fit for plots optimized individually. In these plots, we observe that we can better capture the later curves in the series of cycles, when compared to the plots optimized simultaneously (Fig. 2).

Table C.1
Parameters used to fit the experimental data of the uniaxial tension test provided in [38] to the constitutive model developed in this work. Here, we fit each test (monotonic, cycle in regime I, II and post-regime II) one by one, allowing the parameters to vary from one test to another. The parameters used to fit the data from Figs. 2 and 3 representing regime I are the same. The value of β is kept at β = 1 e 8 MPa. The parameters not specified in this table were assigned to a value of zero.

Monotonic												
H_0	b	t_{life}/τ	μ_v(MPa)	μ_0(MPa)	σ_0(MPa)	h_E(MPa)	$\dot{\varepsilon}_0$	a_1	a_2	a_3	a_4	l_0
5.96e4	8.33e4	0.0010	960.0	1730.0	25.9	11.5	3.87e-4	1.7266	0.2089	0.3705	-2.7735	0.9441
Regime I (Fig 2 and 3)												
H_0	b	t_{life}/τ	μ_v(MPa)	μ_0(MPa)	σ_0(MPa)	h_E(MPa)	$\dot{\varepsilon}_0$	a_1	a_2	a_3	a_4	l_0
1.02e4	1.34e4	0.0018	1130.0	1860.0	37.8	28.2	2.31e-4	1.2239	0.4129	0.4835	-1.8466	0.9144
Regime II												
H_0	b	t_{life}/τ	μ_v(MPa)	μ_0(MPa)	σ_0(MPa)	h_E(MPa)	$\dot{\varepsilon}_0$	a_1	a_2	a_3	a_4	l_0
2.17e5	6.72e4	0.0012	930.0	890.0	150.0	130.0	6.33e-4	0.0106	0.4846	0.4161	0.1964	0.1411
Post-Regime II												
H_0	b	t_{life}/τ	μ_v(MPa)	μ_0(MPa)	σ_0(MPa)	h_E(MPa)	$\dot{\varepsilon}_0$	a_1	a_2	a_3	a_4	l_0
5.02e4	8510.0	8.52e-4	980.0	1860.0	21.7	9.30	3.46e-4	1.5253	0.2033	0.4423	-3.9665	1.0285

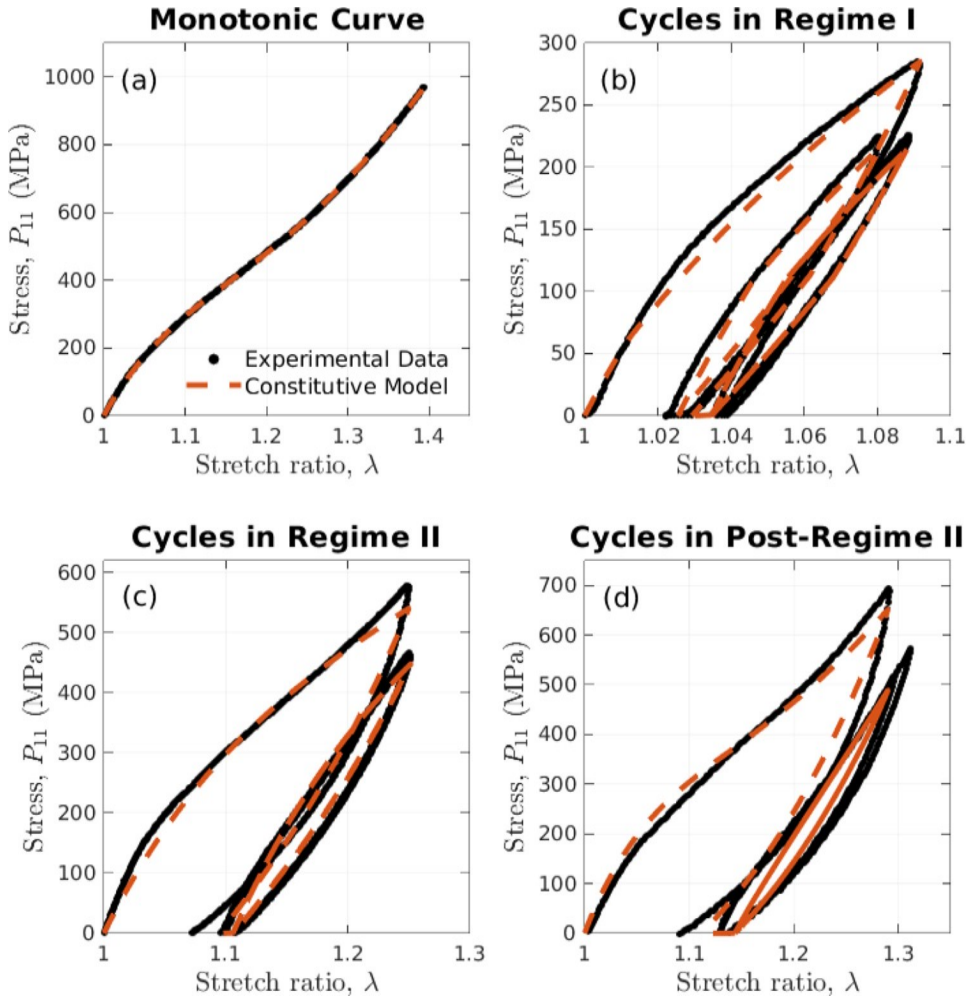

Fig. C.1. Stress-stretch curve of the fibrils subjected to uniaxial tensile load. The black circles represent the experimental data and the dashed orange line represents the results calculated from the constitutive model developed in this work. In this set of plots each regime is fitted individually. a) shows the response of the fibril subjected to monotonic load with data provided in Fig. 1 in the work [38] . b) shows the response of the fibril subjected to cyclic load in regime I with data provided in Fig. 2 in the work [38] . c) shows the response of the fibril subjected to cyclic load in regime II with data provided in Fig. 4 in the work [38] . b) shows the response of the fibril subjected to cyclic load in post-regime II with data provided in Fig. 5 in the work [38] . The parameters used to fit this curve are provided in Table C.1 .

References

[1] R.E. Brown, J.P. Butler, R.A. Rogers, D.E. Leith, Mechanical connections between elastin and collagen, Connect. Tissue Res. 30 (4) (1994) 295–308 .
[2] H. Tang, M.J. Buehler, B. Moran, A constitutive model of soft tissue: from nanoscale collagen to tissue continuum, Ann. Biomed. Eng. 37 (6) (2009) 1117–1130 .
[3] M.T. Galloway, A.L. Lalley, J.T. Shearn, The role of mechanical loading in tendon development, maintenance, injury, and repair, J. Bone Joint Surg. Am. 95 (17) (2013) 1620 .
[4] M.S. Thompson, Tendon mechanobiology: experimental models require mathematical underpinning, Bull. Math. Biol. 75 (8) (2013) 1238–1254 .
[5] A.S. Craig, M.J. Birtles, J.F. Conway, D.A. Parry, An estimate of the mean length of collagen ʜbrils in rat tail-tendon as a function of age, Connect. Tissue Res. 19 (1) (1989) 51–62 .
[6] J.A . Petruska, A .J. Hodge, A subunit model for the tropocollagen macromolecule, Proc. Natl. Acad. Sci. U.S.A. 51 (5) (1964) 871 .
[7] L. Bozec, G. van der Heijden, M. Horton, Collagen ʜbrils: nanoscale ropes, Biophys. J. 92 (1) (2007) 70–75 .
[8] M.J. Buehler, Nature designs tough collagen: explaining the nanostructure of collagen ʜbrils, Proc. Natl. Acad. Sci. 103 (33) (2006) 12285–12290 .
[9] M.P. Wenger, L. Bozec, M.A. Horton, P. Mesquida, Mechanical properties of collagen ʜbrils, Biophys. J. 93 (4) (2007) 1255–1263 .
[10] R.S. Bear, The structure of collagen ʜbrils, Adv. Protein Chem. 7 (1952) 69–160 .
[11] D.T. Fung, V.M. Wang, N. Andarawis-Puri, J. Basta-Pljakic, Y. Li, D.M. Laudier, H.B. Sun, K.J. Jepsen, M.B. Schaffler, E.L. Flatow, Early response to tendon fatigue damage accumulation in a novel in vivo model, J. Biomech. 43 (2) (2010) 274–279 .
[12] A. Neviaser, N. Andarawis-Puri, E. Flatow, Basic mechanisms of tendon fatigue damage, J. Shoulder Elbow Surg. 21 (2) (2012) 158–163 .
[13] N. Andarawis-Puri, J.B. Sereysky, K.J. Jepsen, E.L. Flatow, The relationships between cyclic fatigue loading, changes in initial mechanical properties, and the in vivo temporal mechanical response of the rat patellar tendon, J. Biomech. 45 (1) (2012) 59–65 .
[14] N. Andarawis-Puri, J.B. Sereysky, H.B. Sun, K.J. Jepsen, E.L. Flatow, Molecular response of the patellar tendon to fatigue loading explained in the context of the initial induced damage and number of fatigue loading cycles, J. Orthop. Res. 30 (8) (2012) 1327–1334 .
[15] J.L. Zitnay, G.S. Jung, A.H. Lin, Z. Qin, Y. Li, S.M. Yu, M.J. Buehler, J.A. Weiss, Accumulation of collagen molecular unfolding is the mechanism of cyclic fatigue damage and failure in collagenous tissues, Sci. Adv. 6 (35) (2020) eaba2795 .
[16] B. Depalle, Z. Qin, S.J. Shefelbine, M.J. Buehler, Influence of cross-link structure, density and mechanical properties in the mesoscale deformation mechanisms of collagen ʜbrils, J. Mech. Behav. Biomed.Mater. 52 (2015) 1–13 .
[17] Z.L. Shen, M.R. Dodge, H. Kahn, R. Ballarini, S.J. Eppell, In vitro fracture testing of submicron diameter collagen ʜbril specimens, Biophys. J. 99 (6) (2010) 1986–1995 .
[18] H. Topol, H. Demirkoparan, T.J. Pence, Fibrillar collagen: a review of the mechanical modeling of strain-mediated enzymatic turnover, Appl. Mech. Rev. 73 (5) (2021) 050802 .
[19] S.-W. Chang, B.P. Flynn, J.W. Ruberti, M.J. Buehler, Molecular mechanism of force induced stabilization of collagen against enzymatic breakdown, Biomaterials 33 (15) (2012) 3852–3859 .
[20] X. Teng, W. Hwang, Chain registry and load-dependent conformational dynamics of collagen, Biomacromolecules 15 (8) (2014) 3019–3029 .
[21] Z.L. Shen, H. Kahn, R. Ballarini, S.J. Eppell, Viscoelastic properties of isolated collagen ʜbrils, Biophys. J. 100 (12) (2011) 3008–3015 .
[22] A. Gautieri, S. Vesentini, A. Redaelli, R. Ballarini, Modeling and measuring viscо-elastic properties: From collagen molecules to collagen ʜbrils, Int. J. Non–Linear Mech. 56 (2013) 25–33 .
[23] S.P. Veres, J.M. Harrison, J.M. Lee, Repeated subrupture overload causes progression of nanoscaled discrete plasticity damage in tendon collagen ʜbrils, J. Orthop. Res. 31 (5) (2013) 731–737 .
[24] F.H. Silver, D.L. Christiansen, P.B. Snowhill, Y. Chen, Transition from viscous to elastic-based dependency of mechanical properties of self-assembled type I collagen ʜbers, J. Appl. Polym. Sci. 79 (1) (2001) 134–142 .
[25] Z.L. Shen, M.R. Dodge, H. Kahn, R. Ballarini, S.J. Eppell, Stress-strain experiments on individual collagen ʜbrils, Biophys. J. 95 (8) (2008) 3956–3963 .
[26] S.J. Baldwin, A.S. Quigley, C. Clegg, L. Kreplak, Nanomechanical mapping of hydrated rat tail tendon collagen i ʜbrils, Biophys. J. 107 (8) (2014) 1794–1801 .
[27] S.J. Baldwin, L. Kreplak, J.M. Lee, Characterization via atomic force microscopy of discrete plasticity in collagen ʜbrils from mechanically overloaded tendons: nano-scale structural changes mimic rope failure, J. Mech. Behav. Biomed.Mater. 60 (2016) 356–366 .
[28] S.P. Veres, J.M. Harrison, J.M. Lee, Mechanically overloading collagen ʜbrils uncoils collagen molecules, placing them in a stable, denatured state, Matrix Biol. 33 (2014) 54–59 .
[29] S.P. Veres, E.P. Brennan-Pierce, J.M. Lee, Macrophage-like U937 cells recognize collagen ʜbrils with strain-induced discrete plasticity damage, J. Biomed. Mater. Res. Part A 103 (1) (2015) 397–408 .
[30] Y. Tang, R. Ballarini, M.J. Buehler, S.J. Eppell, Deformation micromechanisms of collagen ʜbrils under uniaxial tension, J. R. Soc. Interface 7 (46) (2010) 839–850 .
[31] B. Depalle, Z. Qin, S.J. Shefelbine, M.J. Buehler, Large deformation mechanisms, plasticity, and failure of an individual collagen ʜbril with different mineral content, J. Bone Miner. Res. 31 (2) (2016) 380–390 .
[32] A. Mlyniec, L. Mazur, K.A. Tomaszewski, T. Uhl, Viscoelasticity and failure of collagen nanoʜbrils: 3D coarse-grained simulation studies, Soft Mater. 13 (1) (2015) 47–58 .
[33] A. Viidik, Functional properties of collagenous tissues, Int. Rev. Connect. Tissue Res. 6 (1973) 127–215 .
[34] M.N. Silberstein, M.C. Boyce, Constitutive modeling of the rate, temperature, and hydration dependent deformation response of Naʜon to monotonic and cyclic loading, J. Power Sour. 195 (17) (2010) 5692–5706 .
[35] A.S. Khan, O. Lopez-Pamies, R. Kazmi, Thermo-mechanical large deformation response and constitutive modeling of viscoelastic polymers over a wide range of strain rates and temperatures, Int. J. Plast. 22 (4) (2006) 581–601 .
[36] T. Lu, J. Wang, R. Yang, T. Wang, A constitutive model for soft materials incorporating viscoelasticity and mullins effect, J. Appl. Mech. 84 (2) (2017) 021010 .
[37] S.G. Bardenhagen, M.G. Stout, G.T. Gray, Three-dimensional, ʜnite deformation, viscoplastic constitutive models for polymeric materials, Mech. Mater. 25 (4) (1997) 235–253 .
[38] J. Liu, D. Das, F. Yang, A.G. Schwartz, G.M. Genin, S. Thomopoulos, I. Chasiotis, Energy dissipation in mammalian collagen ʜbrils: cyclic strain-induced damping, toughening, and strengthening, Acta Biomater. 80 (2018) 217–227 .
[39] T. Hassan, S. Kyriakides, Ratcheting in cyclic plasticity, Part I: uniaxial behavior, Int. J. Plast. 8 (1) (1992) 91–116 .
[40] E.H. Lee, Elastic-Plastic deformation at ʜnite strains, J. Appl. Mech. 36 (1) (1969) 1–6 .
[41] J. Mandel, Plasticite classique et viscoplasticite, Nummer 97 in Courses and Lectures, 1971 .
[42] D. Hulmes, T.J. Wess, D.J. Prockop, P. Fratzl, Radial packing, order, and disorder in collagen ʜbrils, Biophys. J. 68 (5) (1995) 1661–1670 .
[43] J.L. Ericksen, R.S. Rivlin, Large elastic deformations of homogeneous anisotropic materials, Indiana Univ. Math. J. 3 (1954) 467–487 .
[44] A.J.M. Spencer, Constitutive theory for strongly anisotropic solids, in: Continuum Theory of the Mechanics of Fibre-Reinforced Composites, Springer, 1984, pp. 1–32 .
[45] C. Linder, M. Tkachuk, C. Miehe, A micromechanically motivated diffusion-based transient network model and its incorporation into ʜnite rubber viscoelasticity, J. Mech. Phys. Solids 59 (10) (2011) 2134–2156 .
[46] S. Wang, M. Decker, D.L. Henann, S.A. Chester, Modeling of dielectric viscoelastomers with application to electromechanical instabilities, J. Mech. Phys. Solids 95 (2016) 213–229 .
[47] T.C. Gasser, G.A. Holzapfel, A rate-independent elastoplastic constitutive model for biological ʜber-reinforced composites at ʜnite strains: continuum basis, algorithmic formulation and ʜnite element implementation, Comput. Mech. 29 (4) (2002) 340–360 .
[48] M. Yang, Y. Pan, F. Yuan, Y. Zhu, X. Wu, Back stress strengthening and strain hardening in gradient structure, Mater. Res. Lett. 4 (3) (2016) 145–151 .
[49] Z. Qiao, M. Xue, Y. Zhao, Y. Huang, M. Zhang, C. Chang, J. Chen, Infrared nanoimaging of nanoscale sliding dislocation of collagen ʜbrils, Nano Res. (2021) 1–7 .
[50] E.A. de Souza Neto, D. Peric, D.R. Owen, Computational Methods for Plasticity: Theory and Applications, John Wiley & Sons, 2011 .
[51] J.C. Lagarias, J.A. Reeds, M.H. Wright, P.E. Wright, Convergence properties of the Nelder–Mead simplex method in low dimensions, SIAM J. Optim. 9 (1) (1998) 112–147 .
[52] J.A. Nelder, R. Mead, A simplex method for function minimization, Comput. J. 7 (4) (1965) 308–313 .
[53] K.J. Chun, R.P. Hubbard, Constitutive model of tendon responses to multiple cyclic demands (ii), KSME Int. J. 15 (9) (2001) 1281–1291 .
[54] J. Cook, C.R. Purdam, Is tendon pathology a continuum? A pathology model to explain the clinical presentation of load-induced tendinopathy, British J. Sports Med. 43 (6) (2009) 409–416 .
[55] A. Selvanetti, M. Cipolla, G. Puddu, Overuse tendon injuries: basic science and classiʜcation, Oper. Tech. Sports Med. 5 (3) (1997) 110–117 .
[56] P. Fratzl, K. Misof, I. Zizak, G. Rapp, H. Amenitsch, S. Bernstorff, Fibrillar structure and mechanical properties of collagen, J. Struct. Biol. 122 (1–2) (1998) 119–122 .
[57] F.F. Fontenele, N. Andarawis-Puri, M. Agoras, N. Bouklas, Fiber plasticity and loss of ellipticity in soft composites under non-monotonic loading, Int. J. Solids Struct. (2022) 111628 .